Microwave Synthesis and High-Mobility Charge Transport of Carbon-Nanotube-in-Perovskite Single Crystals

Zhensheng Lyu, Chen Zhao, Jialin Yang, Changxu Liu, Chun-Ho Lin, Jiyun Kim, Tengyue He, Long Hu, Feng Li, Yuting Zhuo, Yansong Shen, Kewei Liu*, Weili Yu*, Tom Wu**

Z. Lyu, Dr. C.H. Lin, J. Kim, T. He, Dr. L. Hu, Prof. T. Wu
School of Materials Science and Engineering, University of New South Wales (UNSW), Sydney, NSW 2052, Australia
E-mail: tom.wu@unsw.edu.au

Dr C. Liu
Faculty of Physics, Ludwig Maximilians University of Munich (LMUM), Munich, 80539, Germany

Dr. Y. Zhuo, Dr. Y. Shen
School of Chemical Engineering, University of New South Wales (UNSW), Sydney, NSW 2052, Australia
E-mail: y.zhuo@unsw.edu.au

C. Zhao, Dr. W. Yu
The Photonics Laboratory, Changchun Institute of Optics, Fine Mechanics, and Physics (CIOMP), Chinese Academy of Science (CAS), Changchun City, 130033, China
E-mail: weili.yu@ciomp.ac.cn

J. Yang, Dr. K. Liu
State Key Laboratory of Luminescence and Applications(SKLLA), Changchun Institute of Optics, Fine Mechanics, and Physics (CIOMP), Chinese Academy of Science (CAS), Changchun City, 130033, China
E-mail: liukw@ciomp.ac.cn

Dr. F. Li
College of Physical Science and Technology, Sichuan University (SA), Chengdu 610064, People's Republic of China

Keywords: hybrid perovskite, single crystal, SWCNT, microwave, carrier mobility, photoresponse

Organolead trihalide perovskites have emerged as a new class of competitive solution processed semiconductors due to their unique combination of optimal optoelectronic properties.

However, poor ambient stability and charge transport are the Achilles' heel of hybrid perovskites limiting their applications. In this work, microwave-assisted synthesis is applied for the first time to rapidly grow perovskite single crystals embedded with single-wall carbon nanotubes (SWCNTs). These nanotube-in-perovskite single crystals are endowed with a carrier mobility one order of magnitude higher than the pure counterpart and an ultrafast photo-response speed (5 ns and 80 ns for rise and decay time, respectively). The fast uniform heating of microwave irradiation facilitates the synthesis of ambient-stable crystals with nanoscale additives, paving the way to creating a wide range of mixed-dimensional perovskite-based nano-composites with optimal properties and device performance.

In the past decade, organic-inorganic hybrid perovskites, especially the methylammonium lead trihalides ($MAPbX_3$), have received a lot of attentions due to their extraordinary physical properties and ease of solution processing. Perovskite-based devices experienced a rapid development and their performance has been significantly improved. The efficiency of hybrid perovskite solar cells has soared from 3.9%[1] to 25.2%[2] in the last decade. Hybrid perovskites have excellent potential in optoelectronic applications due to their unique merits such as bandgap tunability, high absorption coefficient, long carrier diffusion length and economic solution processing.[3-5] However, there are still some issues limiting the further applications of hybrid perovskites, such as poor ambient stability[6] and large-area device reliability.[7] Moreover, the carrier mobility of hybrid perovskites is much lower than that of conventional inorganic semiconductors such as Si, Ge and GaAs. For example, mobility of $MAPbBr_3$ and $MAPbI_3$ single crystals is 25 $cm^2/(V{\cdot}s)$ and 67 $cm^2/(V{\cdot}s)$, respectively, as measured using the space charge limited current (SCLC) technique.[8] In comparison, polycrystalline Si has mobility on the order of 100 $cm^2/(V{\cdot}s)$, and the electron mobility in

intrinsic Si single crystals can reach 1450 $cm^2/(V·s)$.[9] Furthermore, the low-temperature carrier mobility in heterostructures of compound semiconductors such as GaAs can be as high as $3×10^7$ $cm^2/(V·s)$, which enabled the discovery of fractal quantum Hall effect.[10] Therefore, there is an urgent need to develop high-mobility perovskites while preserving the advantage of solution processing in order to advance perovskite-based electronics.

It remains a grand challenge to improve the intrinsic charge transport and carrier mobility in hybrid perovskites because solution processing often leads to high defect densities and charge scatterings. One effective strategy is to couple perovskites with another high-mobility semiconductor, e.g., graphene and single-wall carbon nanotube (SWCNT), in precursor solutions. Such a strategy has been demonstrated to work well in realizing high-performance graphene–inorganic semiconductor nanocomposites.[11] In our previous works, we reported perovskite/SWCNT phototransistors with ultrahigh photo responsivity (1×10^4 $A·W^{-1}$) and detectivity (3.7×10^{14} Jones).[12] In another recent work, we demonstrated that embedding high-purity semiconducting-SWCNT in mixed cation perovskite thin-film transistors improves hole mobility comparable with single crystals and decreases operation voltage (V_{oc}) to 3 V.[13] In a pioneering work, Zeng's group fabricated a flexible photodetector based on $CsPbBr_3$ nanosheet/CNT nanonets composite film, which also exhibited much enhanced responsivity (31.1 $A·W^{-1}$).[14] Furthermore, embedding CNT films as hole-transporting layer or conducting electrodes in perovskite solar cells has also been reported.[15-19]

The electronic performance of polycrystalline perovskite films often suffered from poor surface coverage and charge scattering at grain boundaries.[20-24] It is a consensus that single crystal is a better platform to reveal the intrinsic properties of functional materials. For example, the trap density of perovskite single crystal was shown to be five orders lower than that of polycrystalline films.[25] Furthermore, there has been a few recent reports on incorporating

semiconductor nanomaterials into perovskite single crystals to enhance the functionalities. In a pioneer work, Sargent and co-workers reported that adding lead chalcogenide colloidal quantum dots into halide perovskite single crystal could improve the optoelectronic properties and the air stability due to the atom-scale crystalline coherence.[26-27] However, it remains a grand challenge to explore other value-adding nanomaterials that can be incorporated into perovskite single crystals.

In this work, we report a new reliable microwave-based method to synthesize SWCNT-embedded hybrid perovskite single crystals. The numerical simulation results of the heat transfer revealed that microwave radiation produces fast uniform heating and facilitates the growth of high-quality perovskite single crystals with heterogeneous incorporation of SWCNTs. Structural analysis revealed that the microwave-assisted growth method led to greater crystallinity of single crystals than the conventional contact heating. The carrier mobility of $MAPbBr_3$/SWCNT single crystals with a SWCNT concentration of 0.002 wt.% reaches 298 $cm^2/V{\cdot}s$, which is much higher than that of pure counterpart (25 $cm^2/V{\cdot}s$). The high-mobility charge transport was leveraged to achieve an ultrafast photo-response speed of 80 ns, underscoring the potential of such carbon-nanotube-in-perovskite single crystals in optoelectronic applications.

In the heterogeneous synthesis of composite-type single crystals, one main obstacle is that the conventional crystal growth methods such as inverse temperature crystallization (ITC) takes hours to grow samples with mm-scale dimensions, during which the aggregation of additives like SWCNTs leads to inhomogeneous distribution in the perovskite single crystals. In order to speed up the single crystal synthesis and to achieve uniform distribution of SWCNTs, we modified the ITC method by replacing the conventional conduction heating with microwave-assisted heating, which is a low-cost approach and has been applied to a wide range of functional materials.[28-30] Compare with the conduction heating methods, microwave

processing has a few unique advantages. As shown in **Figure 1a**, the conduction heating method transfers thermal energy through temperature gradient between hot plate, container and solution, which inevitably leads to energy loss as well as poor crystal size control. In contrast, microwave radiation heating is hinged on the dynamic movements of dipoles or ions in polar materials under an applied alternating electromagnetic field. Therefore, the microwave irradiation is directly absorbed by solution with a high heating efficiency, and the effectively suppressed temperature gradient in solution can lead to very uniform crystal size dispersion compared to the conventional conduction heating.

High-quality graphene and semiconductor, e.g., ZnSe, SnO_2 and CdTe/CdSe core/shell quantum dots, have been synthesized via microwave in the past decade.[31-34] Microwave-assisted synthesis has emerged as a rapid, facile, environmentally friendly and cost-effective approach, providing narrow particle size distribution.[35] So far, there have been few reports on the microwave-assisted synthesis of halide perovskites. In 2017, Pan *et al.* reported a series of $CsPbX_3$ nanocrystals with narrow particle size dispersion and optimal physical properties synthesized by microwave-assisted method for LED applications.[36] Very recently, sub-minute microwave heating was applied to replace conventional hot plate heating for large-scale hybrid perovskite film annealing process.[37] Huang et al. claimed such efficient heating method can suppress miscellaneous phases formation and improve photovoltaic device performances.

As shown in **Figures 1b and 1c**, the microwave processing resulted in fast synthesis of both $MAPbBr_3$ and $MAPbI_3$ perovskite single crystals with larger average crystal size and more uniform size distribution compare with the hot plate heating. Crystals with dimensions of mm can be synthesized within 30 min, and growth cycles are repeated to increase the crystal size. In contrast, the conduction heating leads to nucleation and growth of crystals with a wider range of size distribution (**Figure 1d**), and discarding the small crystals (<0.5 mm) causes unnecessary waste of precursor materials. To compare the crystallinity, the XRD patterns of

$MAPbBr_3$ single crystals fabricated by hot plate and microwave heating were presented in **Figure 1e**. All samples exhibit sharp peaks, revealing the excellent crystallinity of the crystals.[38] Moreover, the smaller full-width-at-half-maximum (FWHM) of the microwave-prepared sample (0.095°) relative to that of the sample grown via hot plate heating (0.11°) further illustrates the advantage of microwave-assisted synthesis (**Table S2**).

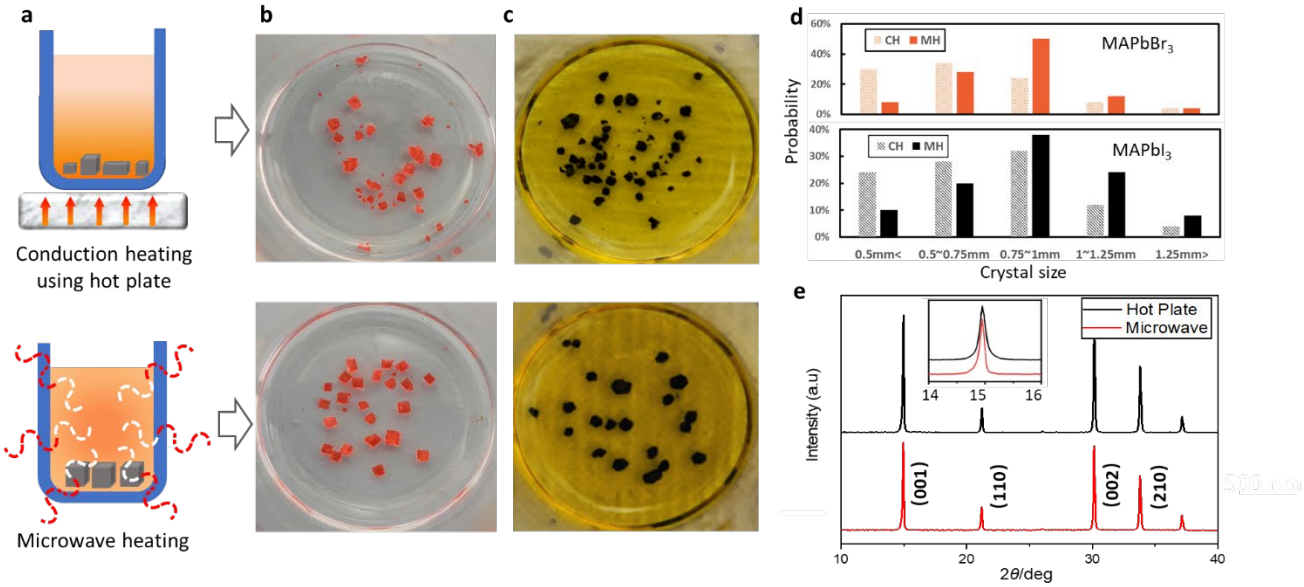

Figure 1. a) Schematics illustrating the conduction heating and microwave heating methods. b) Photos of $MAPbBr_3$ single crystals synthesized by hot plate heating (90 ˚C) and microwave heating (70 W). c) Photos of $MAPbI_3$ single crystals synthesized by hot plate heating (130 ˚C) and microwave heating (70 W). d) Size distributions of pure perovskite single crystals ($MAPbBr_3$ and $MAPbI_3$) synthesized through microwave heating (MH) and conduction heating (CH). e) XRD patterns of $MAPbBr_3$ perovskite single crystals fabricated by microwave heating and hot plate heating methods. The inset compares the (001) peaks of crystals prepared with the two methods.

Furthermore, to shed light on the temperature evolution of the solution under different heating conditions, a 3D transient Computational Fluid Dynamics (CFD) model was developed to simulate the heat transfer process. In this model, the solution is treated as a continuum phase governed by the mass, momentum, and energy conservation equations. The conductive heat transfer and microwave radiation heat transfer are specifically considered. The effect of microwave heating is modelled by magnetohydrodynamics, where the heat source is introduced

based on the imposed external electromagnetic field. The governing equations, the simulation conditions and the relevant nomenclatures are listed in **Tables S3**, **S4**, and **S5**, respectively.

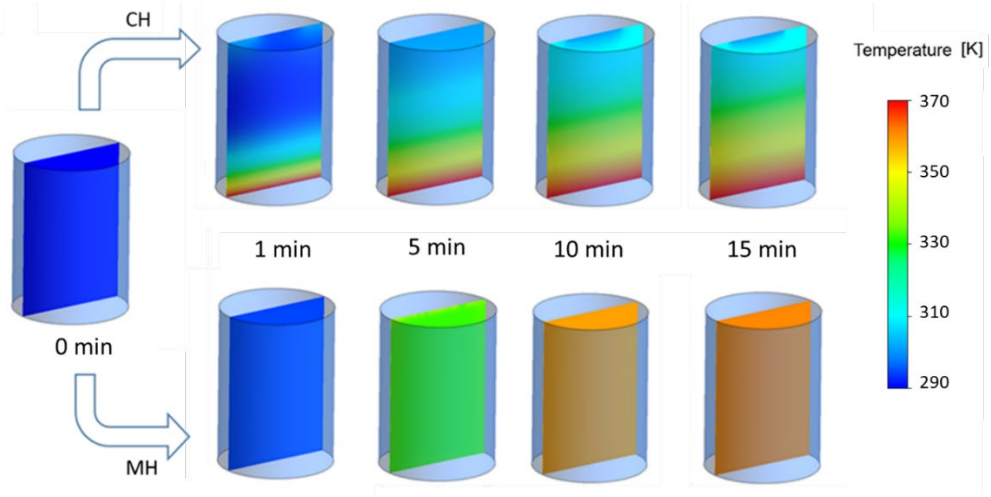

Figure 2. Comparison of the temperature profiles with different heating approaches evolved during the course of 15 min. The heated volume has a diameter of 20 mm and a height of 30 mm. CH and MH represent the conduction heating and the microwave heating, respectively.

Figure 2 shows the comparison of temperature profile evolution in the longitudinal section of the solution container under conductive and microwave heating methods. It can be found that as the heating progresses, the conductive heating always leads to inhomogeneous temperature profiles with the bottom temperature being much higher than the top, which is detrimental for growing large crystals with controlled size. In contrast, the microwave heating produces much uniform temperature distribution profiles. Therefore, microwave heating is favourable for providing efficient and homogeneous heating to facilitate the perovskite crystallization process.

The stability of hybrid perovskite materials is related to many factors including not only the intrinsic ones such as composition and crystallinity but also the extrinsic ones such as moisture, oxidant, light illumination, heat and interface with other materials.[39-42] Most hybrid perovskite-based devices are susceptible to ambient environmental factors due to the hygroscopic nature of organic component and defective sites at grain boundaries. Besides, the

backscattering caused by severe disorders in polycrystalline films negatively modifies the free carrier response.[43] On the contrary, high crystallinity and low defects density has been demonstrated to suppress photo-induced degradation, which underscores the unique advantages of single crystals in reliable device applications.[44] In this work, carbon-nanotube-in-perovskite single crystals showed excellent stability due to the high crystallinity and absence of grain boundary. In this work, we selected $MAPbBr_3$ as the single crystal matrix whose cubic structure keeps perovskite stable under ambient conditions.[45] After four months of exposure to ambient air, there was no obvious colour change observed and the XRD pattern exhibited high crystallinity comparable to fresh single crystals (**Figure S1-2**).

Table 1. Loss tangent δ of some common solvents used in perovskite processing

Solvent	tan δ	Solvent	tan δ
DMSO	0.825	chlorobenzene	0.101
DMF	0.161	chloroform	0.091
Water	0.123	dichloromethane	0.042
ethyl acetate	0.059	toluene	0.040
Acetone	0.054	hexane	0.020

In the design of microwave synthesis, loss tangent tan δ is a key parameter to evaluate microwave absorption of a substance, which determines the transfer efficiency of electromagnetic energy to thermal energy. **Table 1** shows the values of tan δ of several common chemicals used in hybrid perovskite preparation.[46] It is worth noting that DMF, the most widely used solvents for perovskite synthesis, has a quite large value of tan δ, which is advantageous for microwave processing. In addition, rational selection of an additive can help enhance the efficiency of microwave synthesis. Particularly, carbon nanomaterials, such as SWCNT, can significantly facilitate microwave absorption,[47] which presumably accelerates the microwave-assisted synthesis.

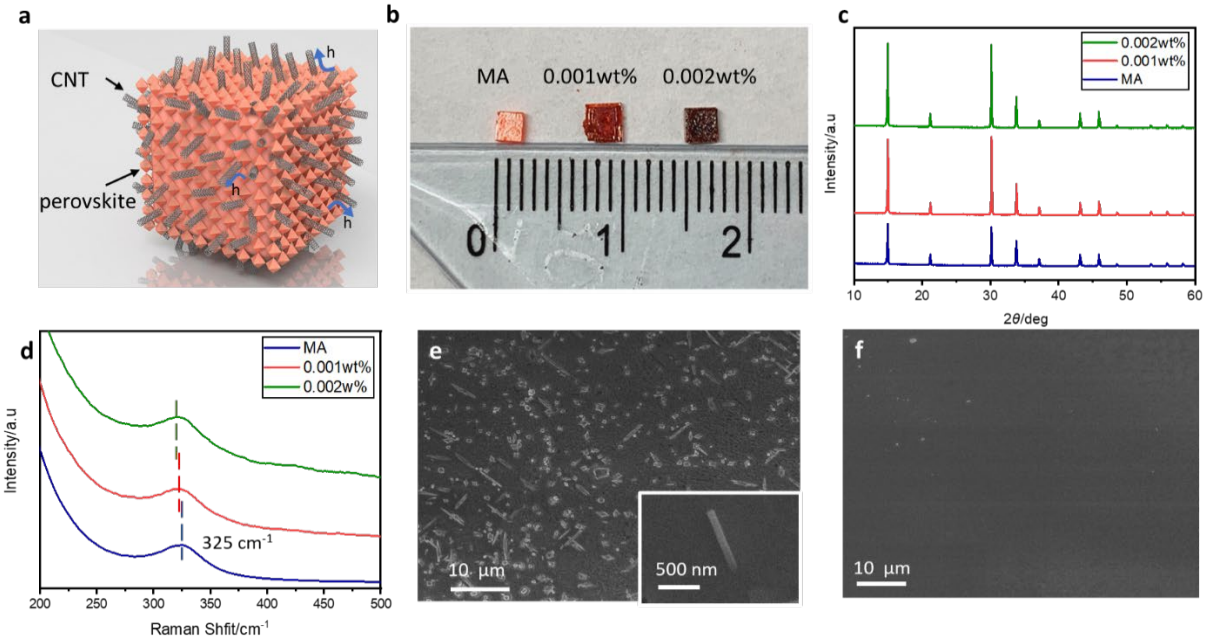

Figure 3. a) Schematic illustration of the tube-in-solid perovskite/SWCNT single crystal. b) Perovskite/SWCNT single crystals synthesized by microwave-assisted heating with different concentrations (0%, 0.001wt.% and 0.002wt.%) of embedded SWCNT. c) XRD patterns of $MAPbBr_3$ and perovskite/SWCNT single crystals. d)The Raman spectra of perovskite/SWCNT single crystals (from 200cm-1 to 500cm-1). Vertical dashed lines marked peaks represent to the MA cation rotation around the C-N axis in perovskite single crystals (in $MAPbBr_3$ is 325 cm^{-1}). e) SEM images of SWCNT-embedded perovskite single crystals and f) pure perovskite single crystals. The insert picture is one single SWCNT bundle.

Embedding SWCNTs in solution-processed polycrystalline films has been shown to improve the performance of perovskite devices.[12] With SWCNTs embedded in hybrid perovskite single crystals, the photo-excited holes in perovskite can transfer to carbon nanotubes which act as high-mobility "highway" for charge transport (**Figure 3a**). The fast growth of perovskite single crystals also ensures uniform dispersion of SWCNTs before their precipitation. It is worth to point out that the solubility of pristine CNT in dimethylformamide (DMF) solution is only 7.9 $mg{\cdot}L^{-1}$. To prepare more stable and homogeneous SWCNTs embedded perovskite single crystals, SWCNT was processed by concentrated acid (HNO_3) before adding into the perovskite precursor solution. This acid treatment modifies the surface carbon atoms and functional groups.[48] As shown in **Figure 3b**, three groups of

$MAPbBr_3$/SWCNT single crystals with 0%, to 0.001wt.% and 0.002wt.% of SWCNTs were fabricated (see Supplementary Information for more synthesis details). The colour of the perovskite single crystals become notably darker with the incorporation of SWCNTs.

We conducted XRD characterization for the perovskite/CNT single crystals, and the results are presented in **Figure 3c**. The SWCNT-embedded crystal exhibits higher peak intensity than the pure counterpart under the same XRD measurement conditions and the FWHM of the (001) peak is also around 0.02° smaller, indicating a better crystallinity as a result of the nanocarbon additive. In addition, the lattice parameter of the SWCNT-embedded samples increased from 5.94 Å to 5.97 Å. Such lattice expansion might indicate the elongation of Pb-X-Pb bond and the relaxation of local lattice strain, which have been demonstrated to benefit the performance of perovskite optoelectronics.[49] The structure of the $MAPbBr_3$/SWCNT single crystals was also investigated using Raman spectroscopy, which provide insights on the structures and properties of both the perovskites and the SWCNTs.[50-54] As shown in **Figure 3d**. the Raman spectra peak of $MAPbBr_3$ around 325 cm^{-1} represents the rotation of MA^+ ions, which has been proved to be relate to the structural stability of hybrid perovskite.[55] Overall, the red shift (from 325 cm^{-1} to 319 cm^{-1}) observed in Raman spectra indicates the elongated lattice parameters, which is consistent with the XRD results.[56]

The morphology of perovskite/SWCNT single crystals was investigated by scanning electron microscope (SEM). As shown in **Figure 3e and f**, in contrast to the smooth surface of the pure perovskite single crystal, the SWCNT-embedded single crystal is featured with "needles" sticking out of the surface, which have diameters in the range of tens of nm and are presumably SWCNT bundles. Besides, the distribution of such SWCNT "needles" appears to quite uniform in the perovskite single crystal. It should be noted here that SWCNT concentrations higher than 0.002wt.% resulted in much thicker SWCNT bundles with

inhomogeneous distribution. Therefore, in this study, we focused on perovskite/SWCNT single crystals with SWCNT concentrations of 0.001wt.% and 0.002wt.%.

The optical and electrical properties of SWCNT-embedded perovskite single crystals were investigated. As shown in **Figure 4a**, the photoluminescence (PL) spectroscopy intensity of 0.002wt.% sample is quenched by approximately three times compared to the pure perovskite sing crystal, which can be attributed to the efficient charge transfer between SWCNT and perovskite and the subsequently suppressed radiative charge recombination. Similar PL quenching was also reported in previous researches on perovskite/CNT thin films.[19] Moreover, PL mapping experiments were carryout out at the peak wavelength of 540 nm. As shown in **Figure 4b**, the PL quenching of perovskite/SWCNT single crystals with SWCNT concentrations of 0.001wt.% and 0.002wt.% appears to be quite homogeneous, which is consistent with the uniform distribution of SWCNTs in the perovskite single crystals.

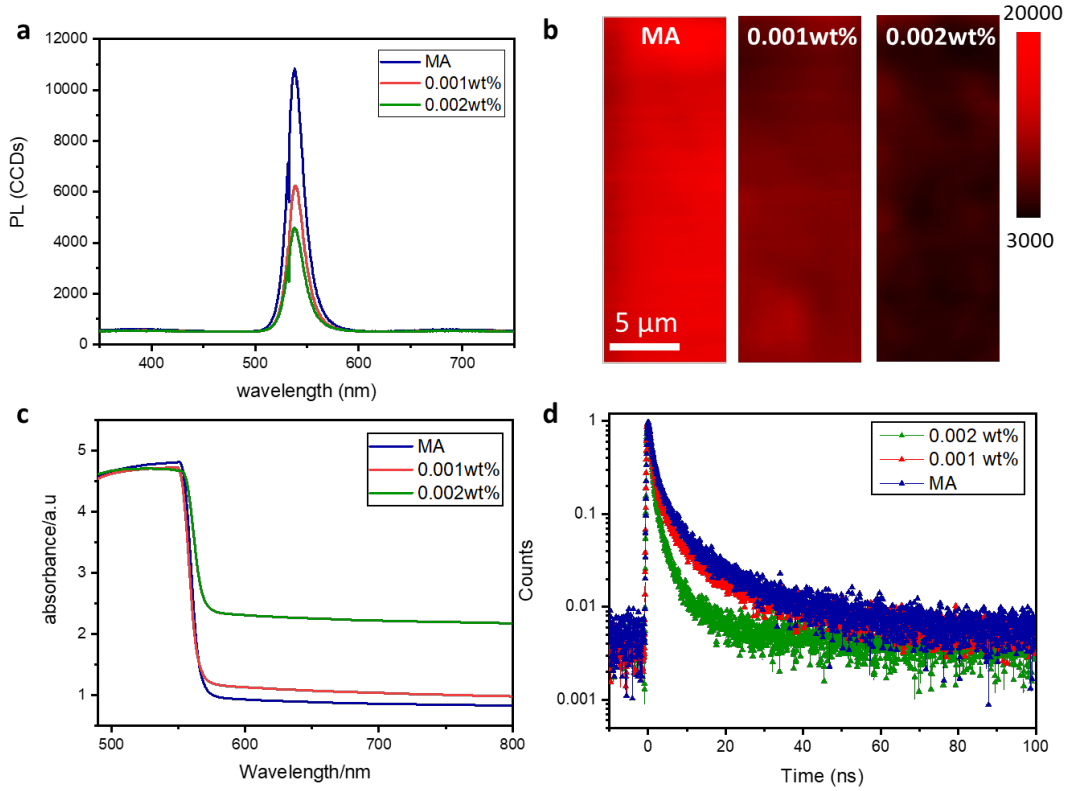

Figure 4. a) The PL quenching observed in photoluminescent spectra of perovskite/SWNT single crystals. b) PL mapping of perovskite/SWCNT single crystals (The numbers on the left represent to PL intensity). c) Absorption spectra of pure and perovskite/SWCNT single crystals.

d) Time resolved photoluminescence of perovskite/SWCNT single crystals with light excitation at 532 nm.

Table 2. Comparison of carrier lifetime extracted from the TRPL data. τ1, τ2 and τ3 represent the lifetimes of excitons, electron-hole pairs and free charge carriers, respectively, and f1, f2, and f3 correspond to their normalized contributions

	τ_1 [ns]	τ_2 [ns]	τ_3 [ns]	f_1	f_2	f_3	$\tau_{average}$ [ns]
MA	1.1624	4.4351	19.62547	0.39998	0.44108	0.15892	5.5402
0.001wt.%	0.8225	2.9213	12.76271	0.52212	0.38127	0.09659	2.7761
0.002wt.%	0.7715	2.9186	12.62597	0.58318	0.32050	0.09631	2.6015

.

Light absorption of different perovskite/SWCNT samples was investigated. The discernible colour variation qualitatively demonstrates the increment of absorption as SWCNT concentration (Fig. 3b). The absorption spectra of pure perovskite and perovskite/SWCNT single crystals are shown in **Figure 4c**. Tauc plots were used to measure the bandgap of perovskite single crystals (Figure S3). The bandgap of perovskite/SWCNT single crystals is 2.19 eV (566nm in wavelength), smaller than that of the pure counterpart (2.21eV). More importantly, at wavelength above 550 nm, the perovskite/SWCNT crystals exhibit enhanced light absorption compared to the pure perovskite, and absorption of photons with energy below the bandgap notably increases with the SWCNT concentration. Such a significant improvement of the light response below bandgap can be ascribed to the broadband light absorption of CNTs.[57-59]

Time-resolved photoluminescence (TRPL) was applied to explore the charge dynamics in SWCNT-embedded perovskite single crystals (**Figure 4d**). The decay curves were fitted to a three-component exponential, which consists of three carrier lifetime components: excitons (τ_1), electron-hole pairs (τ_2) and free charge carriers (τ_3).[60] The carrier lifetimes were given in **Table 2**. Overall, the averaged carrier lifetime of SWCNTs embedded single crystals (2.6 ns) is much shorter than that of pure perovskite (5.5 ns), indicating that SWCNTs significantly

promote the exciton dissociation. The modification of the charge dynamics in the perovskite/CNT crystal suggests efficient generation of free carriers, which can potentially enhance the charge transport in hybrid perovskite single crystals.

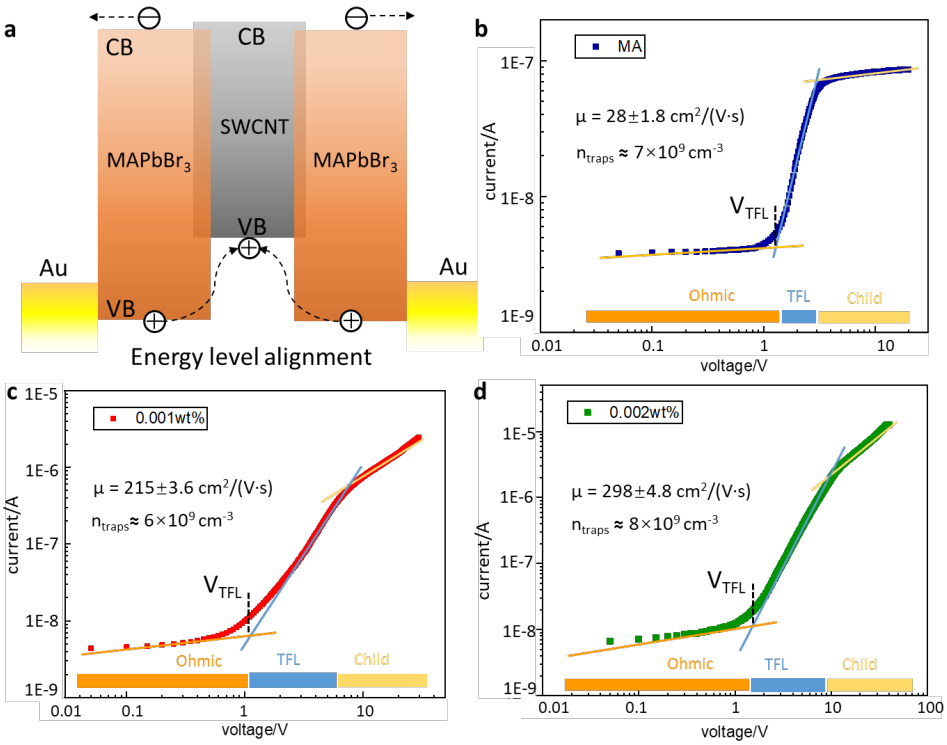

Figure 5. a) the energy band aliment of MAPbBr3 and SWCNT. CB, conduction band; VB, valence band. The I-V curves of b) pure perovskite single crystals, c) 0.001wt.% perovskite/SWCNT single crystals and d) 0.002wt.% perovskite/SWCNT single crystals measured with SCLC in the dark. The regions are marked for Ohmic, TFL and Child's regime. Carrier mobility and trap density are also labelled in the figure.

We further investigated the charge transport properties of nanotube-in-perovskite single crystals. As shown in the energy band diagram (**Figure 5a)**, the perovskite and the SWCNT form a type-II alignment at their interface, i.e., the HOMO of SWCNT (approximately -5.1 eV) is higher than the valence band edge (VBE) of perovskite (-5.5 eV), while the LUMO of SWCNT is also higher than the CBE of perovskite. This kind of band offset causes efficient transfer of photo-generated holes in hybrid perovskite crystals to SWCNTs while leaving electrons behind, subsequently suppressing the charge recombination and enhancing the charge transport.[61] It should be noted that the bandgap of SWCNT is closely related to its diameter

and chirality, which is generally in the range of hundreds of meV.[62] Although we did not explore the impact of the CNT type on the properties of perovskite/CNT crystals, potential property improvements may be realized by judiciously selecting the diameters and chirality of SWCNTs in future works.

In **Figure 5b**, **c** and **d**, the carrier mobility of perovskite semiconductors was evaluated by using the SCLC technique. Au electrodes were evaporated on both sides of the single crystals. In order to avoid high-density interface defects and the associated hysteresis, the crystals should be prepared fresh and properly cleaned using solvent and plasma. The I-V curves exhibit three regimes when the bias increases: ohmic regime ($I \propto V$ n = 1), trap-filled-limit regime (TFL, $I \propto V^n$, n >3) and Child regime ($I \propto V^n$, n = 2). At low voltage bias, the Ohmic current dominates the conductivity, while the excess injection of space charge at high bias will lead to carrier-mobility-dependent SCLC.[63] The transition between these two regimes will occur at trap filling limit region. The carrier mobility μ can be calculated from the Mott-Gurney law:

$$J_D = \frac{9\varepsilon_0\varepsilon_r\mu V^2}{8L^3} \quad (1)$$

where J_D is the dark current, ε_0 represents the vacuum permittivity, ε_r the relative dielectric constant (ε_r = 25.5), ε is the permittivity and L is the sample thickness. Remarkably, μ raises from 23 $cm^2/(V\cdot s)$ for the pristine crystal to 215 $cm^2/(V\cdot s)$ (with 0.001wt.% SWCNTs) and finally reaches 298 $cm^2/(V\cdot s)$ (with 0.002wt.% SWCNTs), indicating that SWCNTs dramatically promote charge transport in perovskite single crystals. Furthermore, the resistivity of the perovskite single crystals decreases by more than one order of magnitude after the incorporation of SWCNTs. The trap density (n_{trap}) can then be determined by the trap-filled limit voltage (V_{TFL}) using the equation

$$n_{\text{trap}} = \frac{2\varepsilon_0\varepsilon_r V_{TFL}}{qd^2} \quad (2)$$

where V_{TFL} is the onset voltage of the trap-filled limit region. As listed in Fig. 5, the trap density is in the range of (6–8) × 10^9 cm^{-3} for the crystals. Clearly, embedding the SWCNTs does not affect much the level of defect trap, and the trap density is several orders of magnitude lower than that of polycrystalline films (10^{15}–10^{17} cm^{-3}), demonstrating the intrinsic merit of single crystals for electronic applications. It is interesting to note that the high carrier mobility in the perovskite/CNT crystals is achieved at a CNT concentration level more than two order of magnitude lower than that reported for thin films [12], indicating a highly effective role of such additives in dictating the charge transport of perovskite single crystals.

To evaluate the photo response of the SWCNT-embedded perovskite crystals, a planar-type photoconductor-type device was fabricated with an active area of 1.8 mm^2. All measurements were conducted under a 2 V voltage bias and the light illumination intensity was 0.02 mW/cm^2. Responsivity is defined as $R = (I_{light} - I_{dark})/P_{light}$, where P_{light} is the light intensity and the I_{light} and I_{dark} represent to the currents under light illumination and in dark. Responsivity of perovskite/SWCNT and pure perovskite devices were measured at different wavelengths and presented in **Figure 6a**. It is worth noting that responsivity depends on multiple factors, such as crystallinity, surface quality, light wavelength and even film thickness.[64-67] Therefore, it can only conclude that the microwave heated pure perovskite device showed reliable responsivity (from 0.04 to 0.43 A/W in wavelength range from 400nm to 800nm) compared to other $MAPbBr_3$ perovskite-based photodetectors.[68-69] Besides, The introduction of CNT facilitates additional absorption for the photons with energy smaller than the bandgap. As a result, moderate responsivity is achieved even at wavelengths of 800 nm (approximately 1 eV). Due to the improved carrier mobility, the responsivity of SWCNT doped single crystal is almost twice higher than pure perovskite single crystals at all wavelength regime, reaching 0.8 A/W (under 0.016 mW/cm^2, 400nm radiation and 2V bias), which also indicates enhanced charge transport in SWCNT-embedded perovskite single crystals. The perovskite-based photo

detector intends to show light intensity-dependent responsivity.[70] As the intensity increases, more photons go deeply into the sample. Consequently, the possibility of reaching the electrodes on top surface for the generated carriers decreases. Such degradation of responsivity was previously reported.[71-72] In this work, as expected, the responsivity of both pure single crystal and SWCNT embedded devices under monochromatic light are inversely proportional to the light intensity, especially in low wavelength regime (< 600 nm).

Furthermore, the photo response properties of SWCNT doped perovskite single crystals under light illumination with different wavelength (from 400 nm to 700 nm) were investigated. The **Figure 6b** presents photo response of perovskite samples illuminated by different wavelength light source for 5 seconds. As expected, the ON/OFF ratios of SWCNT embedded devices keep stable and high between 400nm to 500nm regime. It is well accepted that pure $MAPbBr_3$ based devices showed negligible photo response at higher wavelength regime. On the contrary, compared to pure counterparts, the ON/OFF ratio of SWCNTs embedded devices showed much higher ratios indicating the improvement of light response and absorption derived from carbon nanotube. The variation ON/OFF ratio at different wavelengths matches the responsivity shown in Fig. 6a.

The most notable advantage of perovskite single crystal photoconductor embedded with SWCNT should be its speed since the SWCNT presumably provides the fast tracks for charge transport. Indeed, as shown in **Figure 6c**, the rise time (from 90% to 10%) is 20 ns, 15 ns, and 5 ns, for sample MA, 0.001wt.% and 0.002wt.%, respectively. This response approaches the experimental limit since the pulse width of the pulsed YAG:Nd laser (10 Hz and 540 nm) is 10 ns. We also observed that decay time (from 90% to 10%) remarkably decreased from 0.26 μs (MA) to 0.08 μs (0.002wt.%). All measurements were conducted under a bias of 5 V, and a higher bias may further increase the response speed. To the best of our knowledge, the response speed of the SWCNT-embedded single crystal devices is the fastest among perovskite-based

photodetectors reported so far (**Table S4**, Supporting Information).[40,64,68,73-74] This result suggest that SWCNT-embedded perovskite single crystals provide a promising platform for advancing ultrafast optoelectronic technologies.

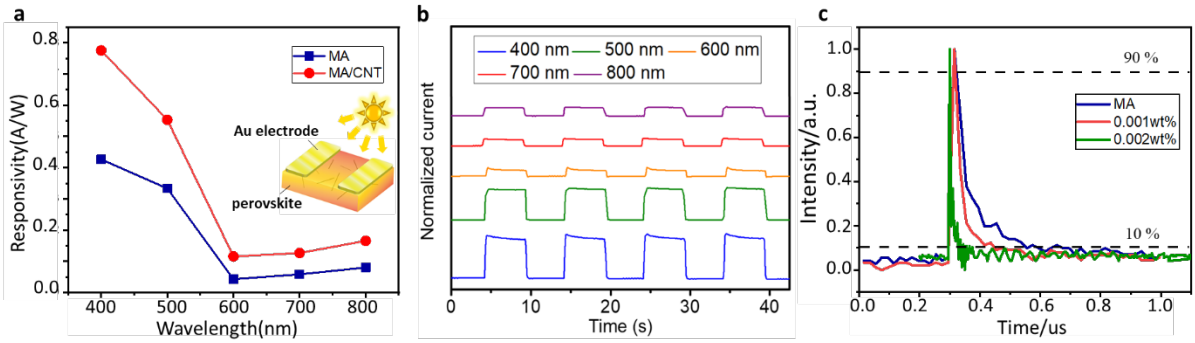

Figure 6. a) Responsivity of the perovskite/SWCNT single crystal devices and the pure counterparts at different wavelengths. Inset is a schematic of the perovskite/SWCNT single crystal photoconductor. b) Normalized light response switching of the perovskite/SWCNT single crystal photodetector at different wavelengths and an intensity of 0.02 mW/cm^2. c) Transient photocurrent curves of the perovskite/SWCNT single crystal photodetector tested with a pulsed YAG:Nd laser.

In summary, this work demonstrates the big potential of microwave-assisted solution-processed perovskite/SWCNT single crystals as a new type of mixed-dimensional optoelectronic materials. With the efficient microwave heating method, the SWCNT-embedded perovskite single crystals exhibit enhanced electrical and optical properties including excellent carrier mobility of 298 cm^2/(V·s), wide-range photo-response and fast operation speed (5 ns and 80 ns for rise and decay time, respectively). These merits can be ascribed to the improved charge transport property of perovskite by embedding SWCNTs, promising for advancing ultrafast broadband optoelectronics.

Experiment section

Perovskite-SWCNTs Solution Preparation: 0.015g SWCNTs with (7,6) chirality (Sigma-Aldrich, >98 wt.%) were processed with 97% HNO_3 at 120°C for 12 h. Then, the SWCNTs were separated in ultracentrifugation machine. After that, oxidized SWCNT was washed with deionized water and centrifuged again. Those steps should be repeated for several times and

then SWCNT was dried in a vacuum oven. Finally, oxidized SWCNT was dissolved in 20ml DMF solution. Methylammonium bromine (MABr) and lead (II) bromine ($PbBr_2$, SigmaAldrich, 98%) were dissolved in DMF (Sigma-Aldrich, 99.8%) with a 1:1 molar ratio to form the 1.2M perovskite precursor solution. To prepare the perovskite/SWCNTs solution, different volume of SWCNT/DMF solution were mixed into the perovskite solution upon sonication for 2 h, corresponding to CNTs/perovskite weight concentration ranging from 0%, 0.001% and 0.002%.

Single Crystal Growth by Microwave Heating: 2 ml perovskite/SWCNTs solution was transferred into 5 ml beakers, and then put into a microwave oven. The processing parameters were chosen as 70 W heating for 1 hr, to get crystal seeds. Then seeds were transferred into new perovskite/SWCNTs solution, heating for 2 hrs with same parameters to obtain methylammonium lead bromine ($MAPbBr_3$) single crystals mixed with SWCNTs.

Simulation of microwave heating: The code was developed based on the framework of ANSYS-FLUENT 2019 R3. The phase coupled semi-implicit method was adopted for pressure-linked equations (PC-SIMPLE). In the PC-SIMPLE method, velocities were solved and coupled by phases. For spatial discretization, the second-order upwind scheme for convective kinematics scheme was applied to discretize the convection term of each scalar. The Green-Gauss cell-based method was applied to estimate the gradients. Under relaxation factors were set to 0.7 for the pressure and momentum equation, and other scalars were set to 0.8. Time discretization was characterized by the CFL number, which was considered under 1.0 so as to improve computational stability and solution convergence. The time step, $t = 10^{-4}$s, and the iteration number per time step, 40, were adopted to enable the residual values to be under 4×10^{-5}. The mesh included around 27,960 cells, which was locally refined in the shear layers. The mesh independence was studied, indicating that a finer mesh (40,000 cells) has

little impact on the simulation results relative to when the coarser mesh was used. Therefore, the present grid resolution was considered to provide accurate results.

Measurements: The XRD was carried out on a MPD (PANalytical) Xpert Multipurpose X-ray Diffraction System using Cu Kα radiation (λ = 1.5406 Å). Both Raman and PL spectra of single crystals were measured on a WITec Alpha300R Confocal Raman Microscope, using an excitation wavelength of 532 nm. The TRPLs were measured on a confocal microscope which consists of a single-photon counting module (SPCM-AQRH-15, Excelitas Technologies), a pulsed supercontinuum laser source (OYSL Photonics, SC-Pro, 150 ps pulse lengths) whose repetition rate is 2 MHz, and a 532 nm long-pass filter. Absorption spectra were recorded using a UV-Vis-NIR spectrophotometer (Cary 5000, Agilent). The morphology images were taken using a field-emission scanning electron microscope (FEI Nova NanoSEM 450). To measure photo-response, Au electrodes with a thickness of 100 nm were deposited on opposite sides of single crystals with scotch tapes as the shadow mask to define the electrode area. The single crystal's charge transport property was characterized using a probe station connected to a Keithley 4200 Semiconductor Parametric Analyzer. The photoexcitation was provided by a wavelength-tunable light source (TLS-55-X300, Sciencetech Inc.) and the light intensity was calibrated using a PM100D power meter (Thorlabs Inc.).

Supporting Information
Supporting Information is available from the Wiley Online Library or from the author.

Acknowledgements
This work was supported by the Australian Research Council (DP190103316).

Received: ((will be filled in by the editorial staff))
Revised: ((will be filled in by the editorial staff))
Published online: ((will be filled in by the editorial staff))

References

[1] A. Kojima, K. Teshima, Y. Shirai, T. Miyasaka, *J. Am. Chem. Soc.* **2009**, *131*, 6050.
[2] Best Research-Cell Efficiencies, https://www.nrel.gov/pv/assets/pdfs/best-research-cell-efficiencies.20200406.pdf (accessed: August 2020).
[3] T. Jeon, S. J. Kim, J. Yoon, J. Byun, H. R. Hong, T. W. Lee, J. S. Kim, B. Shin, S. O. Kim, *Adv. Energy Mater.* **2017**, *7*, 1602596.
[4] X. Hu, X. D. Zhang, L. Liang, J. Bao, S. Li, W. L. Yang, Y. Xie, *Adv. Funct. Mater.* **2014**, *24*, 7373.
[5] F. Wang, H. Yu, H. H. Xu, N. Zhao, *Adv. Funct. Mater.* **2015**, *25*, 1120.
[6] M. I. Asghar, J. Zhang, H. Wang, P. D. Lund, *Renew. Sustain. Energy Rev.* **2017**, *77*, 131.
[7] J. Huang, Y. Yuan, Y. Shao, Y. Yan, *Nat. Rev. Mater.* **2017**, *2*, 17042.
[8] M. I. Saidaminov, A. L. Abdelhady, B. Murali, E. Alarousu, V. M. Burlakov, W. Peng, I. Dursun, L. F. Wang, Y. He, G. Maculan, A. Goriely, T. Wu, O. F. Mohammed, O. M. Bakr, *Nat. Commun.* **2015**, *6*, 7586.
[9] V. A. Fonoberov, A. A. Balandin, *Nano Lett.* **2006**, *6*, 2442.
[10] M. J. Manfra, *Annu. Rev. Condens. Matter* **2014**, *5*, 347.
[11] N. Gao, X. S. Fang, *Chem. Rev.* **2015**, *115*, 8294.
[12] F. Li, H. Wang, D. Kufer, L. L. Liang, W. L. Yu, E. Alarousu, C. Ma, Y. Y. Li, Z. X. Liu, C. X. Liu, N. N. Wei, F. Wang, L. Chen, O. F. Mohammed, A. Fratalocchi, X. G. Liu, G. Konstantatos, T. Wu, *Adv. Mater.* **2017**, *29*, 1602432.
[13] C. Ma, S. Clark, Z. X. Liu, L. L. Liang, Y. L. Firdaus, R. Tao, A. Han, X. G. Liu, L. J. Li, T. D. Anthopoulos, M. C. Hersam, T. Wu, *ACS Nano* **2020**, *14*, 3969.
[14] X. M. Li, D. J. Yu, J. Chen, Y. Wang, F. Cao, Y. Wei, Y. Wu, L. Wang, Y. Zhu, Z. G. Sun, J. P. Ji, Y. L. Shen, H. D. Sun, H. B. Zeng, *ACS Nano* **2017**, *11*, 2015.
[15] S. N. Habisreutinger, R. J. Nicholas, H. J. Snaith, *Adv. Energy Mater.* **2017**, *7*, 1601839.
[16] Q. Luo, H. Ma, F. Hao, Q. Z. Hou, J. Ren, L. L. Wu, Z. B. Yao, Y. Zhou, N. Wang, K. L. Jiang, H. Lin, Z. H. Guo, *Adv. Funct. Mater.* **2017**, *27*, 1703068.
[17] J. Ryu, K. Lee, J. Yun, H. Yu, J. Lee, J. Jang, *Small* **2017**, *13*, 1701225.
[18] I. Jeon, J. Yoon, U. Kim, C. Lee, R. Xiang, A. Shawky, J. Xi, J. Byeon, H. M. Lee, M. Choi, S. Maruyama, Y. Matsuo, *Adv. Energy Mater.* **2019**, *9*, 1901204.
[19] W. Z. Xu, Y. K. Guo, X. T. Zhang, L. Y. Zheng, T. Zhu, D. H. Zhao, W. P. Hu, X. Gong, *Adv. Funct. Mater.* **2018**, *28*, 1705541.
[20] Z. Liu, S. L. Dai, Y. Wang, B. Yang, D. D. Hao, D. P. Liu, Y. W. Zhao, L. Fang, Q. Q. Ou, S. Jin, J. W. Zhao, J. Huang, *Adv. Funct. Mater.* **2020**, *30*, 1906335.
[21] S. N. Habisreutinger, T. Leijtens, G. E. Eperon, S. D. Stranks, R. J. Nicholas, H. J. Snaith, *Nano Lett.* **2014**, *14*, 5561.
[22] S. N. Habisreutinger, T. Leijtens, G. E. Eperon, S. D. Stranks, R. J. Nicholas, H. J. Snaith, *J. Phys. Chem. Lett.* **2014**, *5*, 4207.
[23] Y. C. Shao, Y. J. Fang, T. Li, Q. Wang, Q. F. Dong, Y. H. Deng, Y. B. Yuan, H. T. Wei, M. Y. Wang, A. Gruverman, J. Shielda, J. S. Huang, *Energy Environ. Sci.* **2016**, *9*, 1752.
[24] G. E. Eperon, V. M. Burlakov, P. Docampo, A. Goriely, H. J. Snaith, *Adv. Funct. Mater.* **2014**, *24*, 151.
[25] Q. F. Dong, Y. J. Fang, Y. C. Shao, P. Mulligan, J. Qiu, L. Cao, J. S. Huang, *Science* **2015**, *347*, 967.
[26] M. I. Saidaminov, J. Kim, A. Jain, R. Quintero-Bermudez, H. R. Tan, G. K. Long, F. R. Tan, A. Johnston, Y. C. Zhao, O. Voznyy, E. H. Sargent, *Nat. Energy* **2018**, *3*, 648.
[27] M. X. Liu, Y. L. Chen, C. S. Tan, R. Quintero-Bermudez, A. H. Proppe, R. Munir, H. R. Tan, O. Voznyy, B. Scheffel, G. Walters, A. P. T. Kam, B. Sun, M. J. Choi, S. Hoogland, A. Amassian, S. O. Kelley, F. P. G. de Arquer, E. H. Sargent, *Nature* **2019**, *570*, 96.
[28] U. A. Joshi, J. S. Jang, P. H. Borse, J. S. Lee, *Appl. Phys. Lett.* **2008**, *92*, 242106.
[29] X. H. Zhu, Q. M. Hang, Z. B. Xing, Y. Yang, J. M. Zhu, Z. G. Liu, N. B. Ming, P. Zhou, Y. Song, Z. S. Li, T. Yu, Z. G. Zou, *J. Am. Ceram. Soc.* **2011**, *94*, 2688.
[30] M. P. Selvam, K. J. Rao, *Adv. Mater.* **2000**, *12*, 1621.

[31] H. F. Qian, X. Qiu, L. Li, J. C. Ren, *J. Phys. Chem. B* **2006**, *110*, 9034.
[32] L. M. Sai, X. Y. Kong, *Nanoscale Res. Lett.* **2011**, *6*, 399.
[33] L. B. Tang, R. B. Ji, X. K. Cao, J. Y. Lin, H. X. Jiang, X. M. Li, K. S. Teng, C. M. Luk, S. J. Zeng, J. H. Hao, S. P. Lau, *ACS Nano* **2012**, *6*, 5102.
[34] L. F. Zhu, M. Y. Wang, T. K. Lam, C. Y. Zhang, H. D. Du, B. H. Li, Y. W. Yao, *Sens. Actuators, B* **2016**, *236*, 646.
[35] R. K. Singh, R. Kumar, D. P. Singh, R. Savu, S. A. Moshkalev, *Mater. Today Chem.* **2019**, *12*, 282.
[36] Q. Pan, H. C. Hu, Y. T. Zou, M. Chen, L. Z. Wu, D. Yang, X. L. Yuan, J. Fan, B. Q. Sun, Q. Zhang, *J. Mater. Chem. C* **2017**, *5*, 10947.
[37] Q. Chen, T. T. Ma, F. F. Wang, Y. Liu, S. Z. Liu, J. A. Wang, Z. C. Cheng, Q. Chang, R. Yang, W. C. Huang, L. Wang, T. S. Qin, W. Huang, *Adv. Sci.* **2020**, 2000480.
[38] W. Peng, L. F. Wang, B. Murali, K. T. Ho, A. Bera, N. Cho, C. F. Kang, V. M. Burlakov, J. Pan, L. Sinatra, C. Ma, W. Xu, D. Shi, E. Alarousu, A. Goriely, H. He, O. F. Mohammed, T. Wu, O. M. Bakr, *Adv. Mater.* **2016**, *28*, 3383.
[39] T. Leijtens, G. E. Eperon, N. K. Noel, S. N. Habisreutinger, A. Petrozza, H. J. Snaith, *Adv. Energy Mater.* **2015**, *5*, 1500963.
[40] H. J. Fang, Q. Li, J. Ding, N. Li, H. Tian, L. J. Zhang, T. L. Ren, J. Y. Dai, L. D. Wang, Q. F. Yan, *J. Mater. Chem. C* **2016**, *4*, 630.
[41] W. Y. Nie, H. H. Tsai, J. C. Blancon, F. Z. Liu, C. C. Stoumpos, B. Traore, M. Kepenekian, O. Durand, C. Katan, S. Tretiak, J. Crochet, P. M. Ajayan, M. G. Kanatzidis, J. Even, A. D. Mohite, *Adv. Mater.* **2018**, *30*, 1703879.
[42] X. Wang, Y. C. Ling, X. J. Lian, Y. Xin, K. B. Dhungana, F. Perez-Orive, J. Knox, Z. Z. Chen, Y. Zhou, D. Beery, K. Hanson, J. Shi, S. C. Lin, H. W. Gao, *Nat. Commun.* **2019**, *10*, 695.
[43] C. La-o-vorakiat, T. Salim, J. Kadro, M. T. Khuc, R. Haselsberger, L. Cheng, H. X. Xia, G. G. Gurzadyan, H. B. Su, Y. M. Lam, R. A. Marcus, M. E. Michel-Beyerle, E. E. M. Chia, *Nat. Commun.* **2015**, *6*, 7903.
[44] W. Nie, J. C. Blancon, A. J. Neukirch, K. Appavoo, H. Tsai, M. Chhowalla, M. A. Alam, M. Y. Sfeir, C. Katan, J. Even, S. Tretiak, J. J. Crochet, G. Gupta, A. D. Mohite, *Nat. Commun.* **2016**, *7*, 11574.
[45] M. Shahbazi, H. X. Wang, *Sol. Energy* **2016**, *123*, 74.
[46] B. L. Hayes, *Microwave Synthesis: Chemistry at the Speed of Light*, CEM Publishing, **2002**.
[47] T. J. Imholt, C. A. Dyke, B. Hasslacher, J. M. Perez, D. W. Price, J. A. Roberts, J. B. Scott, A. Wadhawan, Z. Ye, J. M. Tour, *Chem. Mater.* **2003**, *15*, 3969.
[48] T. T. N. Nguyen, S.U.; Phuong, D.T.; Nguyen, D.C.; Mai, A.T., *Adv. Nat. Sci. Nanosci. Nanotechnol.* **2011**, *2*, 035015.
[49] H. Tsai, R. Asadpour, J. C. Blancon, C. C. Stoumpos, O. Durand, J. W. Strzalka, B. Chen, R. Verduzco, P. M. Ajayan, S. Tretiak, J. Even, M. A. Alam, M. G. Kanatzidis, W. Nie, A. D. Mohite, *Science* **2018**, *360*, 67.
[50] K. Nakada, Y. Matsumoto, Y. Shimoi, K. Yamada, Y. Furukawa, *Molecules* **2019**, *24*, 626.
[51] T. Y. Zhang, L. Q. Xie, L. Chen, N. J. Guo, G. Li, Z. Q. Tian, B. W. Mao, Y. X. Zhao, *Adv. Funct. Mater.* **2017**, *27*, 1603568.
[52] S. Costa, E. Borowiak-Palen, M. Kruszynska, A. Bachmatiuk, R. J. Kalenczuk, *Mater. Sci.-Pol.* **2008**, *26*, 433.
[53] M. A. Pimenta, E. B. Hanlon, A. Marucci, P. Corio, S. D. M. Brown, S. A. Empedocles, M. G. Bawendi, G. Dresselhaus, M. S. Dresselhaus, *Braz. J. Phys.* **2000**, *30*, 423.
[54] M. S. Dresselhaus, A. Jorio, A. G. Souza, G. Dresselhaus, R. Saito, *Phys. B: Condensed Matter* **2002**, *323*, 15.
[55] J. H. Lee, N. C. Bristowe, P. D. Bristowe, A. K. Cheetham, *Chem. Commun.* **2015**, *51*, 6434.
[56] T. C. Wei, H. P. Wang, T. Y. Li, C. H. Lin, Y. H. Hsieh, Y. H. Chu, J. H. He, *Adv. Mater.* **2017**, *29*, 1701789.
[57] P. Avouris, M. Freitag, V. Perebeinos, *Nat. Photonics* **2008**, *2*, 341.
[58] V. Perebeinos, P. Avouris, *Nano Lett.* **2007**, *7*, 609.

[59] H. Kataura, Y. Kumazawa, Y. Maniwa, I. Umezu, S. Suzuki, Y. Ohtsuka, Y. Achiba, *Synth. Met.* **1999**, *103*, 2555.
[60] Y. T. Liu, H. Z. Lu, J. X. Niu, H. T. Zhang, S. T. Lou, C. L. Gao, Y. Q. Zhan, X. L. Zhang, Q. Y. Jin, L. R. Zheng, *AIP Adv.* **2018**, *8*, 095108.
[61] P. Schulz, A. M. Dowgiallo, M. J. Yang, K. Zhu, J. L. Blackburn, J. J. Berry, *J. Phys. Chem. Lett.* **2016**, *7*, 418.
[62] C. T. White, D. H. Robertson, J. W. Mintmire, *Phys. Rev. B* **1993**, *47*, 5485.
[63] A. Rose, *Phys. Rev.* **1955**, *97*, 1538.
[64] M. I. Saidaminov, M. A. Haque, J. Almutlaq, S. Sarmah, X. H. Miao, R. Begum, A. A. Zhumekenov, I. Dursun, N. Cho, B. Murali, O. F. Mohammed, T. Wu, O. M. Bakr, *Adv. Opt. Mater.* **2017**, *5*, 1600704.
[65] H. S. Rao, W. G. Li, B. X. Chen, D. B. Kuang, C. Y. Su, *Adv. Mater.* **2017**, *29*, 1602639.
[66] Y. X. Zhang, Y. C. Liu, Y. J. Li, Z. Yang, S. Z. Liu, *J. Mater. Chem. C* **2016**, *4*, 9172.
[67] M. I. Saidaminov, V. Adinolfi, R. Comin, A. L. Abdelhady, W. Peng, I. Dursun, M. Yuan, S. Hoogland, E. H. Sargent, O. M. Bakr, *Nat. Commun.* **2015**, *6*, 8724.
[68] C. X. Bao, Z. L. Chen, Y. J. Fang, H. T. Wei, Y. H. Deng, X. Xiao, L. L. Li, J. S. Huang, *Adv. Mater.* **2017**, *29*, 1703209.
[69] M. Cao, J. Y. Tian, Z. Cai, L. Peng, L. Yang, D. C. Wei, *Appl. Phys. Lett.* **2016**, *109*, 233303.
[70] Y. Zhang, J. Du, X. H. Wu, G. Q. Zhang, Y. L. Chu, D. P. Liu, Y. X. Zhao, Z. Q. Liang, J. Huang, *ACS Appl. Mater. Interfaces* **2015**, *7*, 21634.
[71] Y. C. Liu, Y. X. Zhang, Z. Yang, D. Yang, X. D. Ren, L. Q. Pang, S. Z. Liu, *Adv. Mater.* **2016**, *28*, 9204.
[72] J. X. Ding, S. J. Du, Z. Y. Zuo, Y. Zhao, H. Z. Cui, X. Y. Zhan, *J. Phys. Chem. C* **2017**, *121*, 4917.
[73] W. G. Li, H. S. Rao, B. X. Chen, X. D. Wang, D. B. Kuang, *J. Mater. Chem. A* **2017**, *5*, 19431.
[74] L. T. Dou, Y. Yang, J. B. You, Z. R. Hong, W. H. Chang, G. Li, Y. Yang, *Nat. Commun.* **2014**, *5*, 5404.

Support information

Microwave Synthesis and High-Mobility Charge Transport of Carbon-Nanotube-in-Perovskite Single Crystals

Zhensheng Lyu, Yuting Zhuo, Chun-Ho Lin, Changxu Liu, Jiyun Kim, Tengyue He, Long Hu, Feng Li, Weiyou Yang, Yansong Shen, Kewei Liu*, Weili Yu*, Tom Wu**

In order to investigate the optimal experiment parameters for perovskite/SWCNT single crystals synthesis, various experiments have been carried out. Firstly, the microwave heating efficiency for DMF solution was investigated and results were shown in **Figure S4**The starting temperature was set at room temperature. After heating ten mins, the solution temperature all met the requirement of hybrid perovskite single crystal growth. According to DMF solution heating results, the experiment parameters of SWCNT-in-perovskite single crystals synthesis are listed in the **Table S1**. The heating time represents duration required for full evaporation of solution.

As first, 140W microwave power was chosen to heat precursor solution. Compared to conduction heating, the plunging heating time reveals excellent microwave heating efficiency and crystals immediately appeared in 30s. Moreover, with the addition of SWCNT, the heating time further decreased. However, the unexpected high microwave adsorption of precursors and the selective heating nature of microwave heating led to overheating inside the precursor solution and subsequently boiling of solution. The boiling phenomenon seriously broke the uniformity of liquid phase. The solution splashing results in polycrystalline film with poor surface quality (**Figure S5, b**). Therefore, the priority is to eliminate the boiling phenomenon and synthesize composite materials in a gentler way. In the following experiment, 70W and 140W microwave power was applied for 30s in turns, which effectively retarded boiling

phenomenon. Besides, the larger crystals size suggests that with appropriate processing parameter, synthesis of perovskite single crystals is feasible.

By choosing 70 W microwave power to process precursor solution for 1h, small hybrid perovskite single crystal seeds with 0.8mm size were obtained. Then, crystal seeds were transferred to the pristine precursor solution and heated for another 2 hours to get mm-size perovskite single crystals. It is critical to apply ultrasonic treatment before microwave heating for higher dispersibility of carbon nanotube in SWCNT-perovskite precursor solution (**Figure S6, b**).

It is worth to point out that microwave energy depends on microwave irradiation frequency. So far, all commercial microwave oven can only output 2.45 GHz microwave irradiation. Besides, limited by the steps-like output power levels, it is hard to adjust microwave power to an optimum condition for hybrid perovskite single crystals growth. However, if free-adaptable microwave frequency can be applied in the future, it is reasonable that microwave-assisted heating can be considered as an ideally nanomaterial-in-perovskite composites synthesis method.

Figure S1. The stability of carbon-in-perovskite and pure perovskite single crystals-based photodetectors.

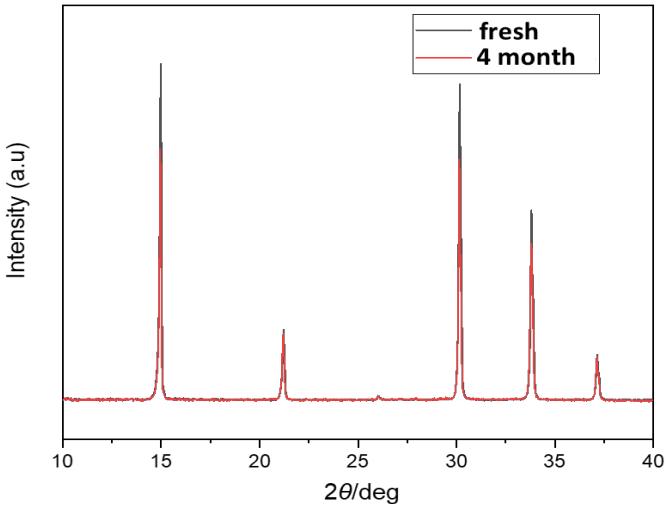

Figure S2. The XRD pattern of pure perovskite single crystals after exposed to ambient air for four months compared with fresh fabricated perovskite.

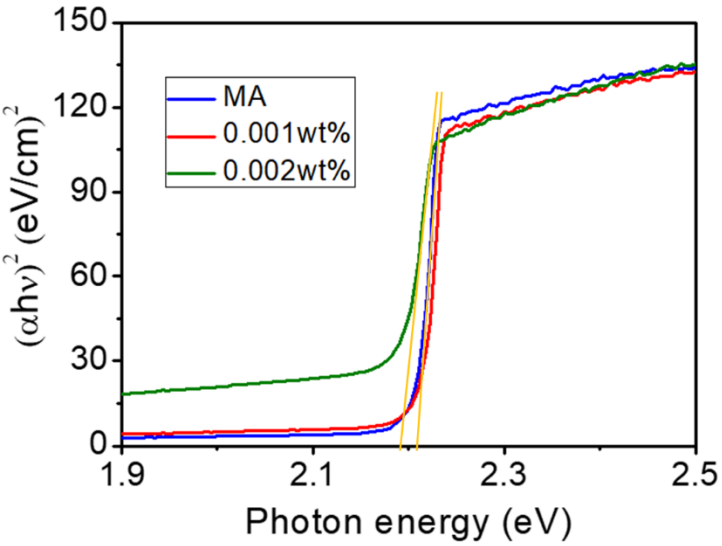

Figure S3. The Tuac plots of pure and mixed perovskite single crystals, indicating corresponding band gap.

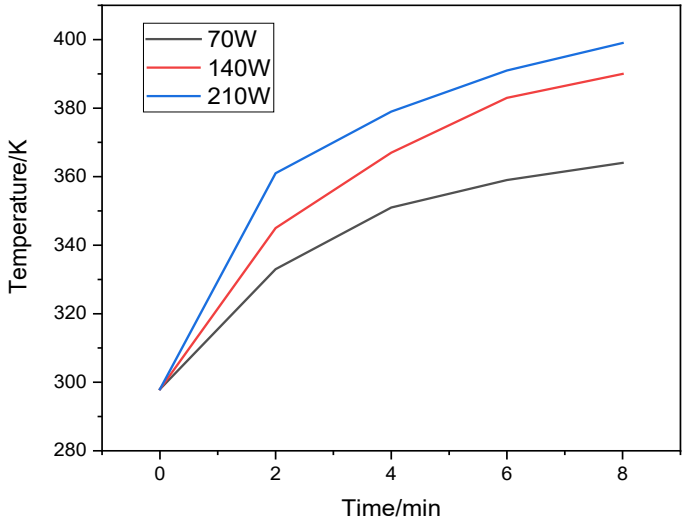

Figure S4 Time-dependent Temperature of DMF heated by microwave oven with different working power.

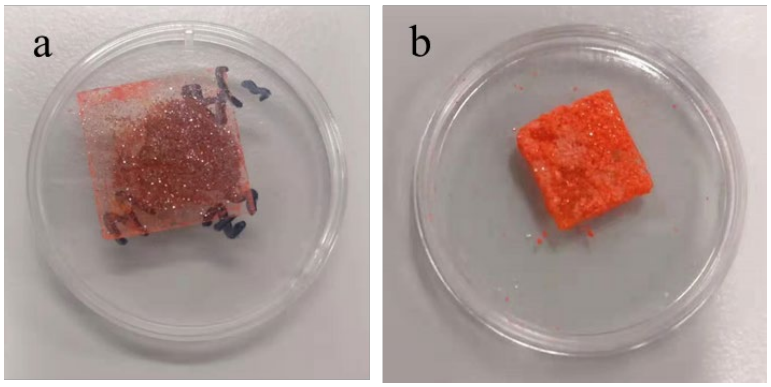

Figure S5 a) SWCNT embedded $MAPbBr_3$ polycrystalline film and b) $MAPbBr_3$ polycrystalline film synthesized by microwave oven in 140W.

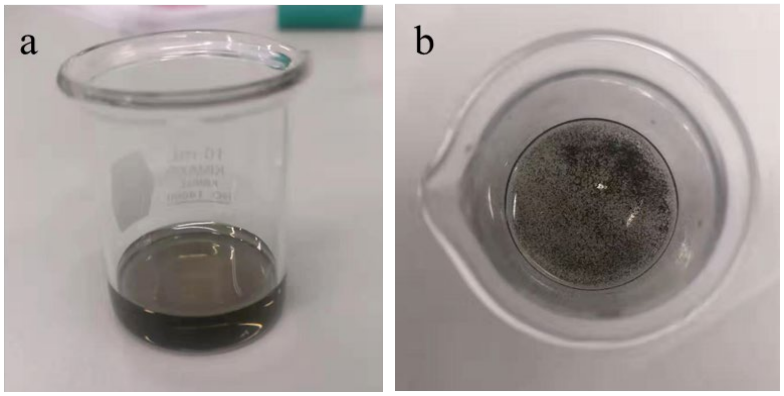

Figure S6 a) SWCNT-perovskite precursor solution after 30min ultrasonic processing; b) SWCNT-perovskite precursor solution without ultrasonic treatment in which obvious aggregation of SWCNT was observe

Table S1. Parameters for preparing perovskite/SWCNT polycrystalline thin films.

Microwave Power [W]	Perovskite precursor solution [ml]	Perovskite solution concentration [Mol.L-1]	SWCNT concentration [wt.%]	Heating Time [min]
140	2	1.0	0	5
140	2	1.2	0	5
70+140	2	1.2	0	10
70+140	2	1.2	0.1	8
70+140	2	1.2	0.2	7

Table S2. FWHM of MAPbBr3 single crystals synthesized by conventional heating and microwave heating respectively.

Crystal indices	(0 0 1)	(1 1 0)	(0 0 2)	(2 1 0)
Hot Plate	0.11°	0.14°	0.13°	0.17°
Microwave	0.095°	0.138°	0.127°	0.148°

Table S3. The governing equation of mass, momentum and energy used in simulating the conduction heating and microwave heating.

$\frac{\partial \rho}{\partial t} + \nabla(\rho \boldsymbol{w}) = \dot{m}$	*mass*
$\frac{\partial(\rho \boldsymbol{w})}{\partial t} + \nabla \cdot (\rho \boldsymbol{w}\boldsymbol{w}) = -\nabla p + \nabla \boldsymbol{\tau} + \rho \boldsymbol{g} + \boldsymbol{S}$	*momentum*
$\frac{\partial}{\partial \mathrm{t}}(\rho \mathrm{E}) + \nabla \cdot (\mathbf{w}(\rho \mathrm{E} + \mathrm{p})) = \nabla \cdot (\mathrm{k}\nabla \mathrm{T} + \boldsymbol{\tau} \cdot \mathbf{w}) + \mathrm{Q}_{\mathrm{rd}}$	*energy*

Table S4. Parameters applied in the simulation.

Density	944 (kg m^{-3})
Specific heat	2140 (J kg^{-1} K^{-1})
Thermal conductivity	0.166 (W m^{-1} K^{-1})
Electrical conductivity	$6e^{-8}$ (Siemens m^{-1})
Solution volume	10 (ml)
Power of microwave oven	70 (W)
Bottom heating temperature	373 (K)
Solution initial temperature	293 (K)

Table S5. Nomenclatures involved in simulation.

ρ	Density (kg m^{-3})
t	Time (s)
w	Velocity (m s^{-1})

$\mathbf{g}$	Gravity acceleration (m s^{-2})
$\dot{m}$	Mass transfer rate (kg m^{-3} s^{-1})
$\boldsymbol{\tau}$	Shear stress tensor (Pa)
$\mathbf{S}$	Momentum Source term (N m^{-3})
p	Pressure (Pa)
Q_{rd}	Intensity of radiation heat exchange (W m^{-3})
T	Temperature (K)
k	Thermal conductivity (W m^{-1} K^{-1})

Table S6. Photo-response speed of perovskite-based single crystal photodetectors in previous reports.

Perovskite	Rising time	Decay time	Ref
$CH_3NH_3PbI_3$	< 0.2 s	< 0.2 s	1
$MA_{0.45}FA_{0.55}PbI_3$	34 μs	164 μs	2
$CH_3NH_3PbI_3$	\	295 ns	3
$CsPbBr_3$	230 ms	60 ms	*4*
$CH_3NH_3PbBr_3$	\	100 ns	5
$CH_3NH_3PbBr_3$		0.12~2.17 ms	6
$CH_3NH_3PbBr_3$	70 μs	150 μs	7
$CH_3NH_3PbCl_3$	24 ms	62 ms	8
$(TMHD)BiBr_5$	9.6 ms	10.3 ms	9
$Cs_3Bi_2I_9$	247μs	230 μs	10
$MAPbBr_3$/SWCNT	5~15 ns	80~260 ns	This work

References

[1] H. J. Fang, Q. Li, J. Ding, N. Li, H. Tian, L. J. Zhang, T. L. Ren, J. Y. Dai, L. D. Wang, Q. F. Yan, *J. Mater. Chem. C* **2016**, *4*, 630.

[2] W. G. Li, H. S. Rao, B. X. Chen, X. D. Wang, D. B. Kuang, *J. Mater. Chem. A* **2017**, *5*, 19431.

[3] Y. T. Liu, H. Z. Lu, J. X. Niu, H. T. Zhang, S. T. Lou, C. L. Gao, Y. Q. Zhan, X. L. Zhang, Q. Y. Jin, L. R. Zheng, *Aip Adv* **2018**, *8*.

[4] M. I. Saidaminov, M. A. Haque, J. Almutlaq, S. Sarmah, X. H. Miao, R. Begum, A. A. Zhumekenov, I. Dursun, N. Cho, B. Murali, O. F. Mohammed, T. Wu, O. M. Bakr, *Adv. Opt. Mater.* **2017**, *5*, 1600704.

[5] C. X. Bao, Z. L. Chen, Y. J. Fang, H. T. Wei, Y. H. Deng, X. Xiao, L. L. Li, J. S. Huang, *Adv. Mater.* **2017**, *29*, 1703209.

[6] Y. T. Liu, H. Z. Lu, J. X. Niu, H. T. Zhang, S. T. Lou, C. L. Gao, Y. Q. Zhan, X. L. Zhang, Q. Y. Jin, L. R. Zheng, *Aip Adv* **2018**, *8*. H. S. Rao, W. G. Li, B. X. Chen, D. B. Kuang, C. Y. Su, Adv. Mater. 2017, 29, 1602639.

[7] P. A. Shaikh, D. Shi, J. R. D. Retamal, A. D. Sheikh, M. A. Haque, C. F. Kang, H. He, O. M. Bakr, T. Wu, J. Mater. Chem. C 2016, 4, 8304.

[8] G. Maculan, A. D. Sheikh, A. L. Abdelhady, M. I. Saidaminov, M. A. Hague, B. Murali, E. Alarousu, O. F. Mohammed, T. Wu, O. M. Bakr, J. Phys. Chem. Lett. 2015, 6, 3781.

[9] C. M. Ji, P. Wang, Z. Y. Wu, Z. H. Sun, L. N. Li, J. Zhang, W. D. Hu, M. C. Hong, J. H. Luo, Adv. Funct. Mater. 2018, 28, 1705467.

[10] W. G. Li, X. D. Wang, J. F. Liao, Y. Jiang, D. B. Kuang, Adv. Funct. Mater. 2020, 30, 1909701.